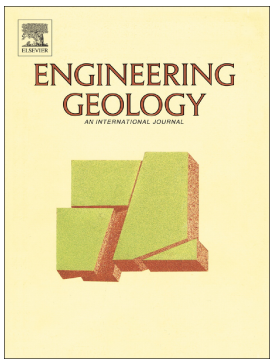

The impact of groundwater drawdown and vacuum pressure on sinkhole development. Physical laboratory models

Xianxuan Xiao, Francisco Gutiérrez, Jesús Guerrero

PII: S0013-7952(20)31791-9

DOI: https://doi.org/10.1016/j.enggeo.2020.105894

Reference: ENGEO 105894

To appear in: *Engineering Geology*

Received date: 8 April 2020

Revised date: 11 September 2020

Accepted date: 28 October 2020

Please cite this article as: X. Xiao, F. Gutiérrez and J. Guerrero, The impact of groundwater drawdown and vacuum pressure on sinkhole development. Physical laboratory models, *Engineering Geology* (2020), https://doi.org/10.1016/j.enggeo.2020.105894

The impact of groundwater drawdown and vacuum pressure on sinkhole development. Physical laboratory models

Xianxuan Xiao[1]*, Francisco Gutiérrez [2], Jesús Guerrero [2]

1. State Key Laboratory of Geohazard Prevention and Geoenvironment Protection, Chengdu University of Technology, Chengdu 610059, Sichuan, China

2. Departamento de Ciencias de la Tierra, Universidad de Zaragoza, C/. Pedro Cerbuna 12, 50009 Zaragoza, Spain

**Corresponding author: Xianxuan Xiao. E-mail: xiaoxianxuan2012@cdut.cn；Tel: +8615882004063*

Abstract

A considerable proportion of the damaging sinkholes worldwide correspond to human-induced subsidence events related to groundwater withdrawal and the associated water-table decline (e.g. aquifer overexploitation, dewatering for mining). Buoyancy loss in pre-existing cavity roofs is generally claimed to be the main underlying physical mechanism. It has been also postulated that rapid water-table drawdowns may create a vacuum effect in the subsurface and contribute to enhance sinkhole activity in karstic terrains with a low effective porosity cover. Our laboratory physical model explores the role played by vacuum pressure induced water-table drops with different magnitudes and rates on sinkhole development, simulating an invariable mantled karst comprising cavernous bedrock and a low-permeability cover. The multiple tests performed include real-time monitoring of the water level drawdown (magnitude, duration, rate), the negative air pressures in the bedrock cavity and the cover, and several features of the subsidence phenomena (deformation style, size, magnitude, rate). The main findings derived from the test results include: (1) Vacuum pressure may trigger the development of

cover collapse sinkholes in areas with low-permeability covers. (2) Different water-table decline patterns (magnitude, duration, rate) may result in different subsidence styles or rheological behaviours: sagging versus collapse. (3) Ground fissuring, frequently related to extension at the margin of sagging depressions, may cancel or significantly diminish the vacuum effect. (4) An overall direct relationship between the water-table decline rate and the subsidence rate. Some possible strategies are proposed to ameliorate the adverse effect of the negative air pressure on sinkhole hazard, which most probably has a local impact restricted by the concurrence of rapid water drawdowns and low-permeability covers.

Keywords: Human-induced sinkhole, Water-table decline, Internal air pressure, Subsidence mechanisms, Subsidence rates

1 Introduction

A significant proportion of the damage related to subsidence activity in karst areas is ascribed to the development of sinkholes induced by various anthropogenic activities. For instance, in China, where the impact of sinkholes has increased dramatically in recent times, around 75% of the damaging subsidence events are classified as human-induced (Lei et al., 2015). Water table decline related to groundwater withdrawal carried out for various purposes (e.g., water supply, dewatering for mining) is one of the main factors involved in the development of human-induced sinkholes in carbonate and evaporite karst regions (e.g., Waltham et al. 2005; Gutiérrez, 2016; Parise, 2019). Since the seminal work published by Newton (1984), most authors explain the increase in sinkhole hazard associated with groundwater level drops to buoyancy loss in the sediments situated above cavities that change from phreatic to vadose conditions (e.g., Lamoreaux and Newton, 1986; Dogan and Yilmaz, 2011; Khanlari et al., 2012; Taheri et al., 2015; Linares et al., 2016; Youssef et al., 2016, 2020; Ali and Choi, 2020). Other physical effects that may contribute to favor ground instability in areas affected by cones of depressions related to water pumping include (Newton, 1984; Gutiérrez et al. 2014): (1) increased hydraulic gradient and accelerated groundwater flow towards the center of the cones depression, which enhance both internal erosion processes and dissolution; (2) the replacement of sluggish lateral flow in a saturated zone, by downward flow percolation in the non-saturated zone, which may accelerate internal erosion processes; (3) repeated oscillations of the water table produce multiple changes in the water content of the sediments, contributing to reduce their mechanical strength.

When the water table declines, the effective porosity occupied by water (e.g., intergranular pores, discontinuities, dissolution voids) is concomitantly replaced by air that mainly permeates from the atmosphere. However, if the water level drop occurs with rapidity and the rate at which the air flows into

the new vadose zone is not high enough to counterbalance the creation of water-free porosity, negative air pressures may occur. The associated vacuum effect is expected to: (1) decrease porosity and cause sediment compaction; and (2) reduce the stability condition of cavities located in the cover and the bedrock, eventually leading to their subsidence (sagging and/or collapse). This vacuum effect has been postulated by a number of authors on the basis of theoretical grounds (Chan, 1988; Chen, 1988; Xu and Zhao, 1988; Waltham, 1989; Guoliang et al., 1990; Chen and Xiang, 1991; Zhou, 1997; Li and Zhou, 1999; Jiang et al., 2015). Some of these authors indicate that the maximum negative pressure is expected to occur at the beginning of the dewatering process, and that the adverse effect on the stability of cavities seems to be especially significant when the water table drops below the cover-bedrock interface. However, to our best knowledge, the causal relationship between the vacuum effect and the development of sinkholes has not been documented with actual quantitative data.

In mantled karst settings, the hydro-mechanical properties of the cover and its thickness play a crucial role on the susceptibility of the ground to sinkhole development, the impact of the water level declines and the style of the subsidence phenomena (Tharp, 1999; Yang and Drumm, 2002; Brinkmann et al., 2008; Song et al., 2012; Nam et al., 2020; Romanov et al., 2020). The latter factor, which largely determines the damaging potential of the sinkholes (severity), is frequently neglected. Cohesionless soils are easily affected by internal erosion (i.e., raveling). Cohesive soils may display a continuous rheological spectrum, from pure brittle deformation (collapse) to ductile deformation (sagging), and these two mechanisms may operate concomitantly and sequentially (Argentieri, 2015; Sevil et al., 2017; Gutiérrez et al., 2018).

The development of sinkholes above cavities can be modeled applying analytical techniques and through physical laboratory models. Augarde et al. (2003) provides a review on the different types of mathematical approaches applied to model the stability of cavities with various geometries and under

different geotechnical conditions (e.g., Tharp, 1999; Keqiang et al., 2004). Published works dealing with physical models are rather scarce and none of them explores the impact of negative air pressures induced by rapid water-table drops. Craig (1990) and Abdulla and Gooding (1996) analyzed the stability of soils over cylindrical cavities through centrifuge modelling, in which overburden weight can be gradually modified by changing the speed of the centrifuge. Lei et al. (2002) briefly present a laboratory model developed in the Institute of Karst Geology of China to assess critical hydro-mechanical conditions for the development of new collapse sinkholes. Poppe et al. (2015) applied computed X-ray microtomography to image subsurface deformation features and monitor subsidence associated with the development of collapse sinkholes in a thick and high-cohesion overburden over cylindrical voids. In this work, we present the results of a physical analog of a cavernous bedrock overlain by a low-permeability cover that allows exploring through real-time monitoring the relationships among (1) variables related to the water-level drawdown (magnitude, duration, rate); (2) vacuum pressure in the cover and the bedrock cavity; and (3) features of the ground subsidence (deformation style, areal extent, magnitude, rate).

2 Experimental installation

The experimental physical analog simulates a covered karst setting in which a low-permeability unconsolidated cover is underlain by cavernous karst bedrock with an opening (e.g., conduit, grike) in the rockhead. The hole connects with a large cavity that has unlimited capacity to hold material derived from the cover by collapse and/or internal erosion processes. The experiment explores the impact of water table declines with different magnitudes and rates, as well as the associated negative air pressures (vacuum or suction effect) on the development of cover-collapse sinkholes. The karst system is reproduced within a geological simulation box 200 cm long, 50 cm wide and 28 cm high (**Fig. 1**). The

cover consists of two layers with constant thickness. The 2 cm thick upper layer is a low-permeability sandy clay, and the 10 cm thick lower layer is made up of higher permeability clayey sand. These layers were prepared for each experiment using the same material and following the same protocol. According to Darcy seepage tests, the hydraulic conductivity of the lower layer (1.25×10^{-2} cm/s) is one order of magnitude higher than that of the upper layer (1.22×10^{-3} cm/s). The main physical properties of the cover layers, including grain-size composition, density, initial moisture content, porosity, hydraulic conductivity, cohesion and angle of friction (clayey sand layer) are indicated in **Table 1**. The rockhead that supports the cover is simulated by a flat and horizontally lying plexiglass plate 1 cm thick. A circular hole 15 cm in diameter located in the plate functions as the opening that connects the cover with the underlying cavity. The position of the center of the hole has a transversal offset of around 7 cm with respect to the geometrical center of the plate. The cavity is simulated in the experiment with a cistern-like space 52 cm high, 191 cm long and 42 cm wide situated below the plexiglass plate. The bottom of the simulation box (i.e., base of the cavity) is considered as the elevation datum (Z=0) for the experiments.

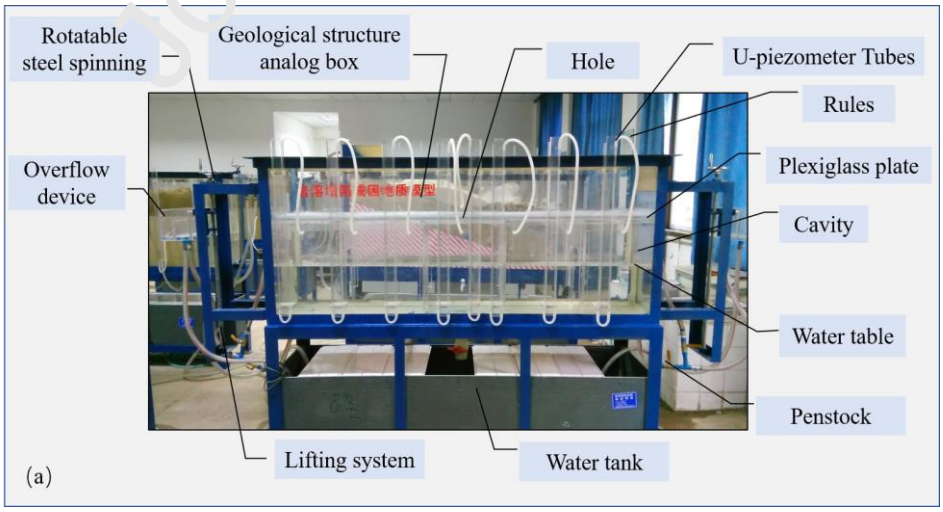

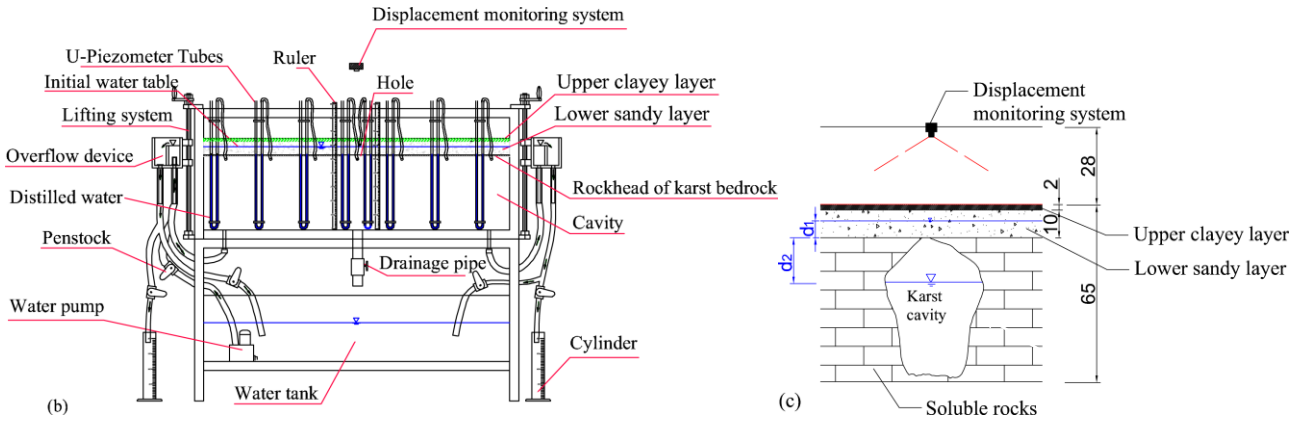

Figure 1. Illustrations of the experimental physical analog. (a) Photograph of the geological simulation box. (b) Sketch of the physical model showing the different components. (c) Idealized representation of the mantled karst setting simulated in the experiments, consisting of an unconsolidated cover with an upper low-permeability clayey seal and karst bedrock hosting a large cavity with an opening at the rockhead. See additional explanations in the text.

The position and vertical variations of the water table are controlled by two overflow systems that follow the communicating vessels concept. They are installed on both sides of the box and can be displaced vertically with rotatable cranks. The overflow systems are connected via several tubes with: (1) a lower water tank (two tubes); (2) the bottom of the karst cavity. The initial incorporation of water into the system is carried out by pumping water from the lower tank and slowly introducing it into the cavity from below, until the water table reaches the level mandated by the overflow device. The water table declines are simulated by lowering the overflow devices up to the desired position, and subsequently allowing the water to drain from the bottom of the cavity towards the lower water tank via the overflow system by opening the corresponding penstocks. The water table drops can be accelerated by opening a drainage pipe situated in the center of the bottom of the cavity (i.e., cistern). Eight U-shaped tubes installed on the side wall of the experimental box measure internal air pressures, seven of them in the

upper part of the cavity and another one in the sandy layer, above the water table. Air pressures are measured with millimetric ruler attached to each U-shaped tube (error margin 0.5 mm).

A fixed laser distanciometer situated above the experimental box is used to measure topographic profiles along the central transverse axis of the experimental box (vertical error margin 0.01 mm). The measuring line covers the area underlain by the hole in the plexiglass plate, which is offset laterally 7 cm (i.e., maximum deformation does not occur in the center). These measurements are used to ensure the horizontal geometry of the top of the cover at the beginning of the experiments, and to monitor vertical displacements related to sinkhole development.

All the experiments start with a stable water table situated at Z=60 cm within the lower sandy unit of the cover (7 cm above the rockhead). The two overflow systems are set at Z=60 cm with the lifting systems. Subsequently, the box is slowly supplied with water at a constant rate from the lower water tank using the pump and through the two tubes situated at the bottom of the cavity. The water level rises slowly and eventually permeates into the sandy cover through the hole in the rockhead until it reaches the desired level. This water level remains stable for several hours before each water-table-decline test is performed. At this stage, the vadose zone includes the upper 3 cm of the sandy layer and the 2 cm thick clayey unit. This upper low-permeability sealing unit prevents effective incorporation of air from above into the interstitial spaces of the cover and the cavity when the water table is dropped at sufficiently high rate, creating negative air pressure (vacuum effect). Obviously, the upper sandy clay unit it is not a perfect seal. Air can flow into the expanding vadose zone of the cover through the soil and along the unsealed boundary between the layer and the wall of the experimental box, with a total length of 466 cm. The air that flows into the cavity when the water table drops below the rockhead has to circulate through the two layers of the cover and converge laterally towards the hole, which functions as a constriction for the flow. At the beginning of the experiments the air pressure in the vadose zone equals the external

atmospheric pressure. In each experiment, the magnitude of the water level drops is controlled by the position of the overflow devices, and their rate can be accelerated by opening the drainage pipe and controlling its outflow rate. The decline of the water level is performed in two steps with variable magnitudes and rates: (1) firstly, the water level descends several centimeters (d1=6-8 cm) up to a position situated at or close to the rockhead; (2) secondly, the water level drops again various magnitudes (d2=6-47 cm) to different levels within the cavity. Details on the selected water-level-decline tests are provided in **Table 2**.

	Grain-size composition	**Density (g/cm^3)**	**Initial moisture content (%)**	**Porosity**	**Hydraulic conductivity (cm/s)**	**Volume weight (kN/m^3)**	**Friction angle (^{o})**	**Cohesion (kPa)**
Upper clayey layer	60% clay, 40% sand	2.15	10	0.176	1.33×10^{-3}	21.5	/	/
Lower sandy layer	20% clay, 80% sand	1.82	8	0.364	1.25×10^{-2}	18.2	33.4	2.68

Table 1 Main physical properties of the cover layers. Hydraulic conductivity and volume weight were measured by the Darcy's Law test and the Wax seal test respectively. The angle of friction and cohesion of the clayey sand layer were obtained from direct shear tests on four samples.

Test number	**Water-level drop (cm)**			**Duration of water-level drop (s)**			**Velocities of water level drop (cm/min)**			**Subsidence style**	**Max. subsidence (mm)**
	d_1	d_2	d_T	T_1	T_2	T_T	V_1	V_2	V_A		
1	6	6	12	1352	1068	2420	0.27	0.34	0.30	No subsidence	0
2	6	7	13	181	1901	2082	1.99	0.22	0.37		0.65
3	7	7	14	144	878	1022	2.92	0.48	0.82	Sagging	0.80
4	6.5	7	13.5	130	720	850	3.00	0.58	0.95		1.50
5	6.5	47	53.5	2106	539	2699	0.18	5.23	1.19	Prolonged sagging with	16.42
6	8	47	55	1740	109	1849	0.28	25.87	1.78	cracking and collapse	18.06
7	6.5	12	18.5	57	718	775	6.84	1.00	1.43	Short sagging and early	11.95+ collapse

8	7	9	16	182	275	457	2.31	1.96	2.10	collapse	6.80+ collapse

Table 2 Details of the eight selected water-level-decline tests comprising two drops (d_1 and d_2) with variable durations (T_1, T_2). The tests are ordered according to the overall average velocity of the water level drops (V_A), from lower to higher. V_A is obtained dividing the total water-level drop (d_T) by the total duration of water-level drop ($T_T=T_1+T_2$).

3 Results

A total of 13 water-level-decline tests were carried. In this work, for brevity, we present the results of the eight most representative ones. They can be grouped into four categories according to the surface deformation pattern and subsidence style, which are related to the magnitude and rate of the water-level drops: (1) Type I: No subsidence; (2) Type II: Sagging; (3) Type III: Prolonged sagging with cracking and collapse; and (4) Type IV: Short sagging and collapse subsidence.

3.1 Type I. No subsidence (Test 1)

In test 1, the water level was dropped 6 cm in each stage ($d_1=d_2=6$ cm) and at slow rates (0.27 and 0.34 cm/min) (**Table 2**). The recorded negative air pressures, like in the rest of the tests, were higher in the cavity than in the vadose zone of the cover. Air inflow rate in the cavity is lower than in the upper part of the sand layer since the air has to circulate along longer distances and across more flow-obstructing-constricting elements (e.g., the full thickness of the cover layers and the hole in the rockhead). As soon as the water level started declining, the negative pressures in both the vadose zone and the cavity increased abruptly and reached a peak (0.53 and 1.36 kPa) in a very short time span (24-37 s) (**Fig. 2**). Then, the negative pressures decreased gradually to reach steady values (0.4 and 1.05 kPa), showing that the effect of the progressive water level decline on air pressure was counterbalanced by air inflow. No surface deformation was recorded in this test, indicating that: (1) the drop of the water table below the rockhead did not produce any significant volume reduction in the cover (i.e.,

consolidation); and (2) the induced stress conditions created by the moderate and slow water table drops were not sufficient to exceed the mechanical threshold values that control the stability of the cover above the hole in the rockhead.

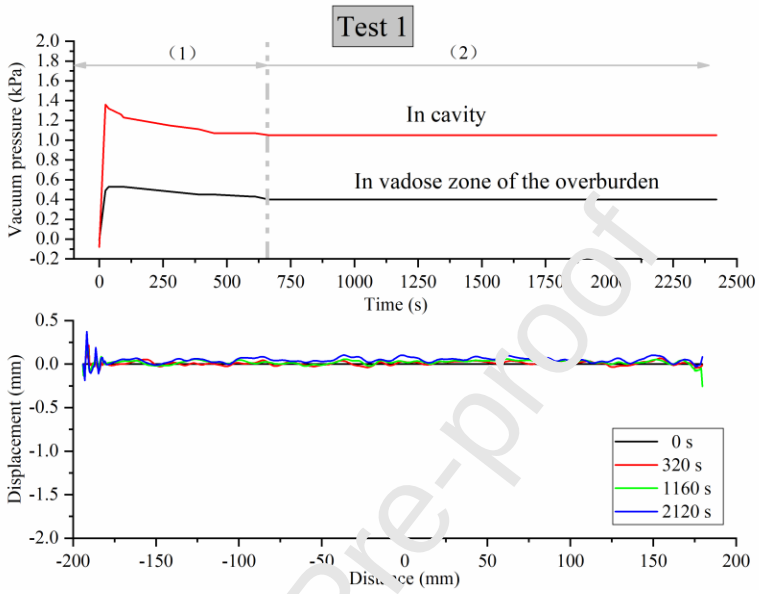

Figure 2. Data from test 1. The upper graph shows the negative air pressure recorded in the cavity and in the upper part of the sandy layer in the course of the water-level decline stages 1 and 2, labelled as (1) and (2). The lower graph shows the topographic profiles recorded at different times (two in stage 1 and two in stage 2), indicating no subsidence. The serrated pattern is related to the error margin of the measurements and the imperfect planar geometry of the ground surface.

3.2 Type II. Sagging (Tests 2, 3, 4)

In tests 2, 3 and 4, the magnitude of the water level drop was 6-7 cm in each stage, similarly to test 1. However, the water table declined at high rates during the first stage of each test; 1.99, 2.92 and 3.00 cm/min in tests 2, 3 and 4, respectively (**Table 2**). The negative air pressures displayed a similar pattern to that of test 1: (1) initial rapid rise up to peak values (peak pressures at cavity 1.64, 1.79, 1.74 kPa); (2) progressive decline during stages 1 and 2; and (3) steady state conditions during approximately the second half of stage 2. The cumulative vertical deformation profiles record subtle sagging above the 15

cm-diameter hole affecting an area around 25-30 cm across. This indicates that deformation widens upwards above the hole with a variable angle of draw of around 26-37° (**Fig. 3**). The deformation profiles show a rather symmetric pattern and the last profiles indicate limited maximum subsidence values of 0.65, 0.8 and 1.5 mm for tests 2, 3 and 4, respectively. Note that the position of the hole has some lateral offset with respect to the geometrical center of the experimental box (i.e., maximum displacement does not coincide with 0 distance). No evidence of cracking was observed in the surface of the cover. Displacement data from test 4 seem to indicate marginal flexural bulging (uplift) in one of the margins of the subsidence depression. Moreover, the basal part of the cover material situated just above the hole did not experience any collapse, as observed through the glass wall of the experimental box.

Subsidence rates have been computed for various time periods considering the vertical displacement at the point of maximum subsidence (**Fig. 3**). These rates reach the highest values during the first water-level-drop stages (5.54×10^{-3}, 37.8×10^{-3}, 13.23×10^{-3} mm/s in tests 2, 3 and 4, respectively), when the decline rates were highest (**Fig. 4**). The subsidence rates decreased during the second decline stages, characterized by slower water table drops. The average subsidence rates in tests 2, 3 and 4 at the point of maximum displacement considering the full temporal length of the experiment were 6.74×10^{-4}, 1.33×10^{-3} and 3.56×10^{-3} mm/s, respectively. Overall, these tests indicate that there is a direct relationship between the water table decline rate and the subsidence magnitude and rate. Test 4 shows some deviation from this general relationship, since peak negative pressure values in the cavity and subsidence rates were lower than in test 3, despite water-level decline rate was slightly higher in test 4. This deviation is probably related to non-identical geological settings simulated at each experiment.

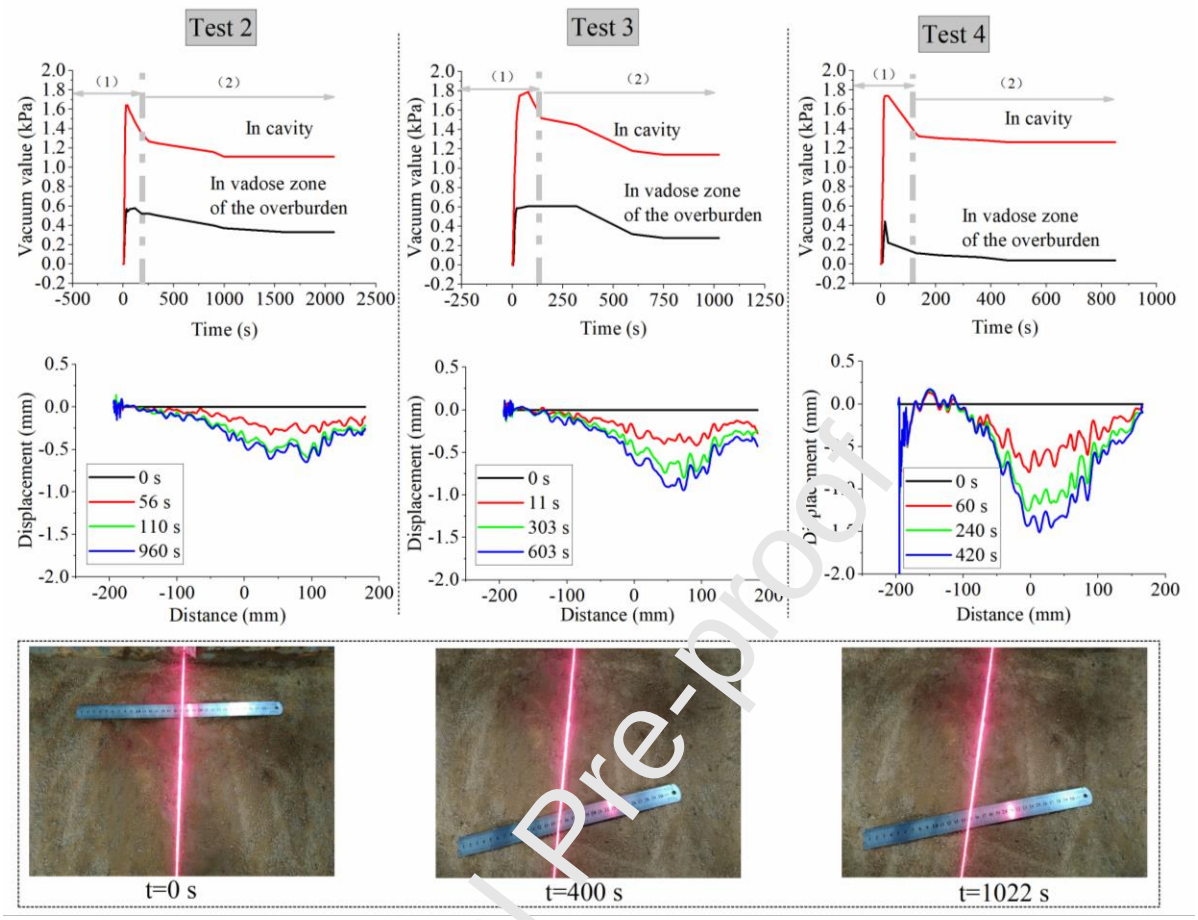

Figure 3. Data from tests 2, 3 and 4 characterized by sagging subsidence. The upper graphs show the negative air pressures recorded in the cavity and in the upper part of the sandy layer during the water-level decline stages 1 and 2. The lower graphs show the topographic profiles recorded at different times showing sagging subsidence and probably marginal bulging in test 4. The sequence of photographs corresponds to images taken at different times of test 3. They show the lack of fissure development during the experiment.

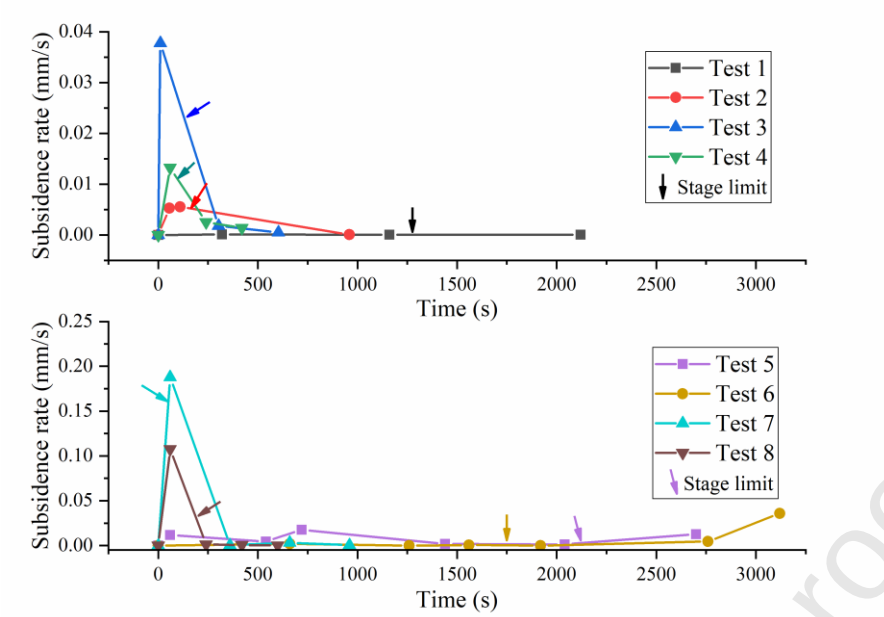

Figure 4. Subsidence rates computed for various time periods considering the vertical displacement at the point of maximum subsidence. Points are located at the end of each time lapse. Upper graphs show data from tests 1 to 4, and lower graph data from tests 5 to 8. Arrows point to boundary between stage 1 and 2.

3.3 Type III. Prolonged sagging with cracking and collapse (Tests 5, 6)

In tests 5 and 6, the water table declines in the first stage were similar to those of the previous tests (6.5 and 8 cm), whereas the second stages were characterized by major drops of 47 cm. The velocities of the water table drop in the first stages were low (0.18 and 0.28 cm/min) and much higher than in the previous tests in the second decline stages (5.23 and 25.87 cm/min) (**Table 2**). Hence these experiments are characterized by large and rapid water table declines in the second stage. At the beginning of the first stage, despite the limited magnitude and rate of the water table drop, a well-defined subcircular crack 11-12 cm in diameter developed on the ground surface. In test 5 negative air pressure in the cavity shows an initial short-lasting peak (1.38 kPa). No or limited negative pressure built up occurred in the

cavity at the beginning of test 6. This can be attributed to the early development of surface fissuring just above the hole that expedites air inflow and negative air pressure compensation. Nonetheless, negative air pressure shows very short and abrupt peaks in the stage 1 of test 6, and in stage 2 of both tests. These vacuum-effect events indicate episodes of inefficient air flow into the cover and the cavity, probably due to temporary closure of the fissures associated with the ongoing deformation process. The cumulative vertical displacement profiles of test 5 show a broad and slightly asymmetric deformation zone 35 cm across dominated by sagging. In stage 2, inner concentric fissures were recorded at the surface and subsidence significantly accelerated in this central part of the subsidence zone. At around 2700 s, once the maximum subsidence had reached 16.42 mm (average subsidence rate 0,0061 mm/s) (**Fig. 5**), a collapse nested in the inner zone of the subsidence depression occurred. In test 6 ground deformation was spatially more restricted (11 cm across). In stage 2 subsidence accelerated and was accompanied by the development of new concentric cracks associated with the negative pressure peak (**Fig. 4**). At around 3120 s, once the maximum subsidence had reach 18.06 mm (average subsidence rate 0,0058 mm/s), a rapid collapse formed. In both tests, subsidence rate shows accelerations associated with the larger and more rapid water table drops of stage 2.

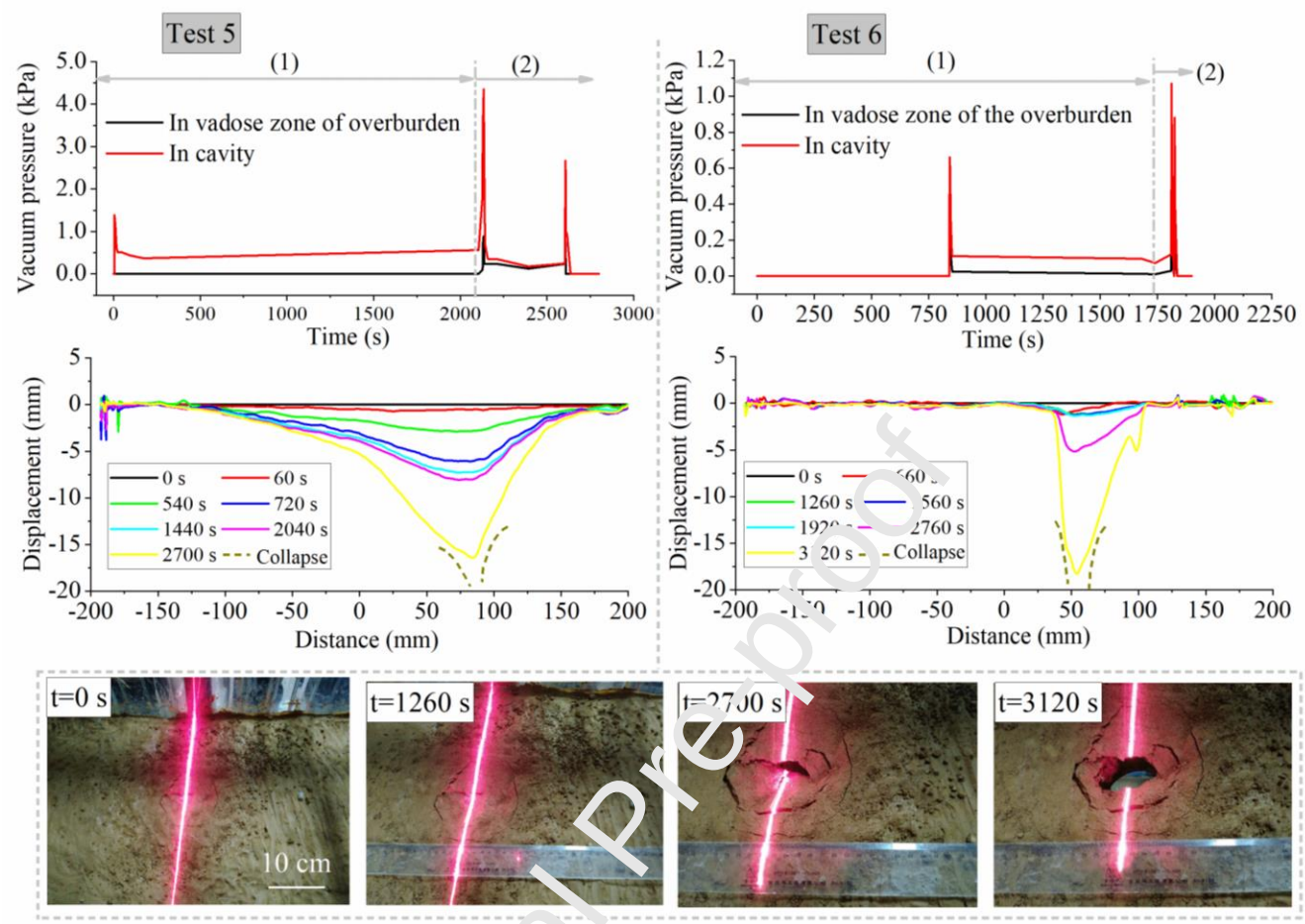

Figure 5. Data from Tests 5 and 6 characterized by prolonged sagging with cracking and collapse. The upper graphs show the negative air pressures recorded in the cavity and in the upper part of the sandy layer during the water-level decline stages 1 and 2. The lower graphs show the topographic profiles recorded at different times before the development of the final collapse. The sequence of photographs corresponds to images taken at different times of Test 6.

3.4 Type IV. Short sagging and early collapse (Test 7, 8)

In tests 7 and 8 the magnitudes of the water table declines were low to moderate in the first stage (6.5 and 7 cm) and in the second stage (12 and 9 cm). The water level was dropped at high rates in both stages, especially in the first stage of test 7 (6.84 cm/min) (**Table 2**). At the beginning of both tests, a rapid rise in the negative air pressure was recorded in both the cavity and the vadose zone of the cover. Peak values were reached much faster in test 7, in which the velocity of the water table decline was

much higher (6.84 cm/min versus 2.31 cm/min). Subsequently, negative pressures fell slightly and remained at high values both in the cavity (ca. 0.8 kPa) and in the cover (**Fig. 6**). Immediately after the start of the tests the ground surface was affected by rapid sagging in a subcircular area 24-26 cm in diameter. Subsidence rates peaked in the first stage, reaching 187.7×10^{-3} and 107.6×10^{-3} mm/s in tests 7 and 8, respectively (**Fig. 4**). In stage 2 sagging continued but at a very low rate, despite the rapid water table decline. The fact that no fissures formed on the ground surface explains the sustained high negative pore pressures. These discontinuities provide pathways for the air to flow into the cover and the cavity and contribute to compensate the suction effect of the water table decline. Eventually, nested collapse sinkholes 3 and 4.5 cm across with overhanging edges formed in the center of the sagging depressions, accompanied by an abrupt fall-to-zero in the negative air pressures (**Fig. 6**). The average subsidence rates in tests 7 and 8 at the point of maximum displacement considering the time span of experiment before the collapse were 12.45 $x10^{-3}$ and 11.3[illegible] $x10^{-3}$ mm/s, respectively.

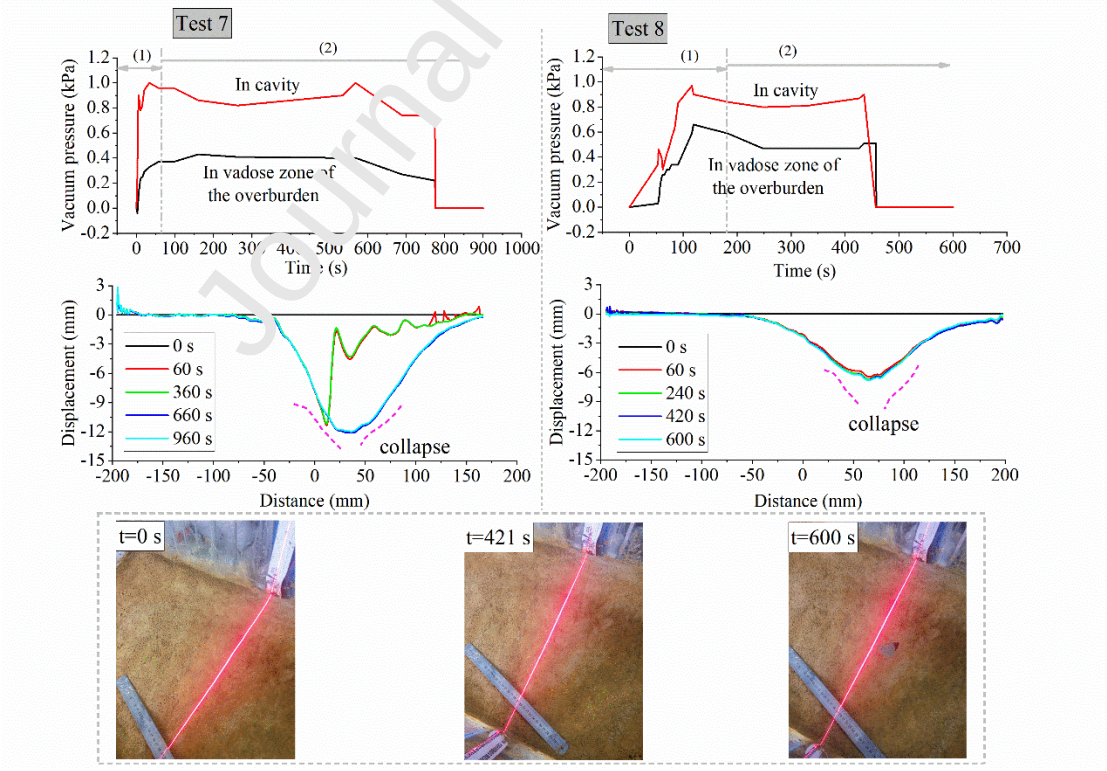

Figure. 6 Data from tests 5 and 6 characterized by prolonged sagging with cracking and collapse. The upper graphs show the negative air pressures recorded in the cavity and in the upper part of the sandy layer during the water-level decline stages 1 and 2. The lower graphs show the topographic profiles recorded at different times before the development of the final collapse. The sequence of photographs corresponds to images taken at different times of test 8.

4 Discussion

The multiple tests carried out with the physical model that simulates sinkhole development in a low-permeability cover underlain by cavernous bedrock include real-time monitoring of the water level drawdown (magnitude, duration, rate), the negative air pressure in the bedrock cavity and the cover, and several features of the subsidence process (deformation style, size, magnitude, rate). These data illustrate that rapid water table declines and the resulting high negative air pressures may induce subsidence in settings with a low permeability cover. Although, the characteristics of the cover are essentially invariable, there are complex inter-relationships between the magnitude and rate of the water-level decline, the resulting negative air pressures, and several features of the ground subsidence. The deformation style and subsidence rates are largely dependent on water-level decline rates. Moreover, the subsidence mechanisms and the rheology of the cover, notably the formation of fissures that function as permeability features, have a significant impact on both negative air pressure and the final collapse event.

4.1 Vacuum pressure and surface fissuring

The majority of the tests show that vacuum pressure reaches the maximum value almost instantaneously after the onset of the water level decline, due to initial lag in the air replenishment process (e.g. Figs. 2 and 3). Negative air pressures are lower in the cover than in the cavity, since air has to circulate along a longer path and through a higher number of obstructing and constricting elements.

Subsequently, vacuum pressures drop and tend to stabilize, indicating some balance between the continuing water-level drawdown and the rate of air inflow (e.g., Figs. 2 and 3). Capillary tension in the clayey sand layer most probably has a very limited mechanical effect, due to its sand-dominated texture, and the fact that the water level decline is accompanied by a downward air flow within the cover layer, that tends to replenish the drained porosity. The situation changes abruptly when throughgoing cracks and fissures develop in the cover. These permeability features speed up the air inflow. The vacuum pressure drops to null or residual values in the cover, but may remain relatively high in the deeper cavity (Fig. 5). As a result, the suction effect still operates at the base of the cover (i.e., cavity roof) and the subsidence process continues. After the initiation of surface fissuring, negative pressures in the cover and the cavity may experience sharp and short-lasting peaks (Fig. 5). These discrete events of lower air inflow may be attributed to the temporary closure of fissures, which develop coevally with the sagging of the cover.

4.2 Stability threshold and subsidence style

In test 1, characterized by reduced and slow water-level drops, no subsidence occurred, despite negative pressures were recorded in both the cavity and the cover (Fig. 2). This fact has two implications: (1) the buoyancy loss related to the water table drop in our experiments is insufficient to induce subsidence; (2) vacuum pressure needs to surpass a threshold value for subsidence to initiate. In tests 2 and 6, the cover sagged despite water-level decline rates and negative pressures were similar or slightly lower than those of test 1 (Figs. 3, 5). This suggests that the threshold values may slightly change due to the non-perfectly equal conditions for the different tests.

The different tests reveal that the deformation style of the cover and its temporal evolution is influenced by the magnitude and especially the rate of the water-level drops. However, the number of

tests performed is probably insufficient to fully understand these complex relationships. In tests 2, 3 and 4, characterized by reduced but rapid water-level drops in stage 1 (1.99-3.00 cm/min), subsidence is characterized by very slow sagging with limited magnitude and without the development of ground fissures (Figs. 3, 4, 7). The water-level drawdown in this case was rapid, but not long enough to produce significant subsidence. The resulting sagging depression was significantly larger than the underlying hole in the rockhead, indicating a widening-upward ductile deformation zone with an angle of draw within the range of 25-40°. Tests 5 and 6 were characterized by large and rapid water level declines in stage 2. In these tests, despite the reduced magnitude and rate of the drawdown in stage 1, subsidence was initiated by sagging of the cover and the development of marginal cracks. The peripheral fissures may be attributed to radial extension in the margin of the subsidence bowl that counterbalances the centripetal contraction that experiences the cover due to passive bending (e.g., Gutiérrez et al., 2012; Carbonel et al., 2014). As subsidence evolved and the water-level decline rate increased in stage 2, inner concentric cracks developed, subsidence accelerated in the central zone, and eventually a nested collapse formed. The fissure pattern together with observations of the experiments indicate that in these tests, fissuring and collapse faulting was controlled by inward dipping to subvertical failure planes (Fig. 5). Subsidence in these tests displayed a clear episodic pattern, with discrete displacement events correlative to negative pressure peaks (Figs. 5, 7). Subsidence in tests 7 and 8, with rapid water-level declines in both stages, was characterized by rapid sagging subsidence affecting an area larger than that of the underlying hole in the rockhead. Passive bending of the cover was not accompanied by surface fissuring, and hence sustained negative pressures were recorded (Fig. 6). The high stress and strain conditions gave way after a relatively short time span to the development of a small nested collapse sinkhole in the center of the subsidence bowl. The observation of the hole in the experiments, with clear overhanging edges, indicates that they were controlled by outward dipping failure planes, similar to those reported by

Poppe et al. (Poppe, 2015) in their physical experiments. In all the cases, collapses occur when the water table lies below the rockhead and the cover is no longer supported by buoyancy. This indicates that collapse subsidence is favored by both the vacuum effect and buoyancy loss.

4.3 Water-level decline rate and subsidence rate

Monitoring data suggest that water-level decline magnitude does not play a significant role on the subsidence process. In contrast, as expected, there is a clear direct relation between the water-level decline rate and the subsidence rate. The latter parameter refers to vertical displacement rate at the point of maximum subsidence in the center of the sinkhole before the final collapse. Figure 4 shows that the subsidence rates computed for specific time periods reach the highest values during the stages with fastest water-level drawdowns. Figure 7 illustrates that average subsidence rates are higher in the stages with quicker water declines; for instance, stage 2 in tests 5 and 6. The plots of figure 8 show the general dependency between the average subsidence rates and the average water-level decline rates computed for each test. Test 7 plots as an outlier, probably due to anomalous assymmetric subsidence in the initial part of the test (see profiles in Fig. 6). Being the rest of the factors constant, the more rapid the water table drop, the higher the vacuum pressure and consequently the higher the deformation rate. This general relationship may be influenced by other factors in our experiments, such as changes in the permeability of the cover (e.g. fissuring), antecedence or mechanical disturbance of the cover in a previous stage (e.g. strain softening), or non-identical conditions in the different experiments.

Obviously, the results of the laboratory experiments cannot be directly transferred to real natural sinkholes. Although there is considerable geometrical, mechanical and hydrodynamic similarity, there is a large scale deviation. Moreover, the laboratory physical models do not incorporate the common highly heterogeneous nature of mantled karst settings. Cover deposits can have a complex composition and

architecture, the rockhead typically has a pinnacled, not planar geometry, and the openings and permeability features at the cover-bedrock interface can be highly diverse in geometry (e.g., elongated grikes versus subcircular pipes) and distribution (isolated versus clustered). Despite the upscaling limitations from physical laboratory experiments to natural systems, the results of the investigation indicate that negative air pressures induced by rapid water table drawdowns may trigger or accelerate sinkholes. However, this is most probably a secondary and local factor compared to buoyancy loss due to the following reasons: (1) the build-up of vacuum pressures requires the concurrence of both rapid water level declines and a low permeability cover, whereas buoyancy loss operates regardless of the nature of the cover and the speed of the drawdown; (2) in areas affected by groundwater withdrawal and the formation of cones of depressions, negative air pressures may only operate in the vicinity of the pumping points, where the water level decline is more severe and rapid. Our experiments, in agreement with the experience reported in previous works, suggest that the probability for subsidence to be initiated depend significantly on three factors: (1) The exceedance of a threshold value for the negative air pressure, which tends to peak at the beginning of the water-level drop episodes. This threshold value is governed by the mechanical and hydrological properties of the cover and may vary significantly depending on local factors (e.g., size and geometry of cavities). (2) The decline of the water level below the cover-bedrock interface. At this stage buoyancy loss in the cover reaches its maximum value and downward vadose flow can easily undermine its base by collapse and internal erosion processes. (3) The velocity of the water drawdown, which determines the magnitude of the vacuum effect.

Although most probably negative pressure related to groundwater withdrawal has a local effect on the stability of cover sediments in karst terrains, special care should be paid when water pumping is carried out in the vicinity of vulnerable structures (e.g., high-speed railways). According to the factors mentioned above, some possible alternatives for ameliorating its impact may include reducing the water

level decline rates, preventing water level drops below the rockhead, and start the water pumping process in a progressive way, checking for the possible occurrence of instability signs (e.g., fissuring,sagging).

The effect of vacuum pressure on sinkhole development remains as a poorly explored topic. It would be desirable to develop additional physical experimental models incorporating other factors, such as covers with variable permeability and thickness or holes with other geometries (elongated grikes). The vacuum effect could be also investigated by means of coupled mechanical-hydrological computer simulations. Of special interest would be to monitor natural karst settings with impervious clayey covers in which water pumping could be accompanied by negative pressures.

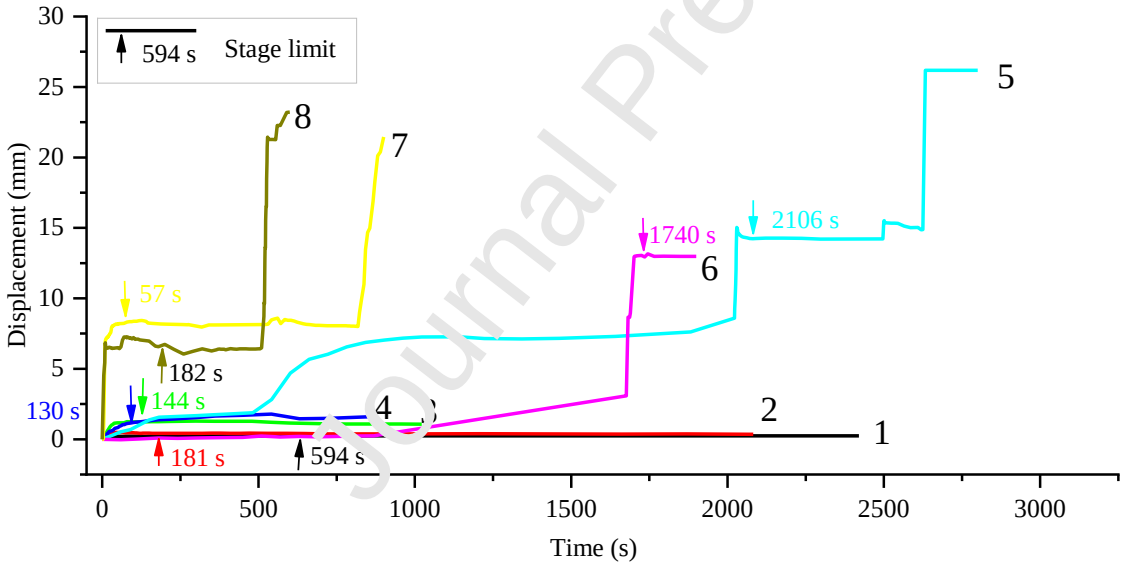

Figure 7. Plot showing cumulative displacement versus time for the different tests.

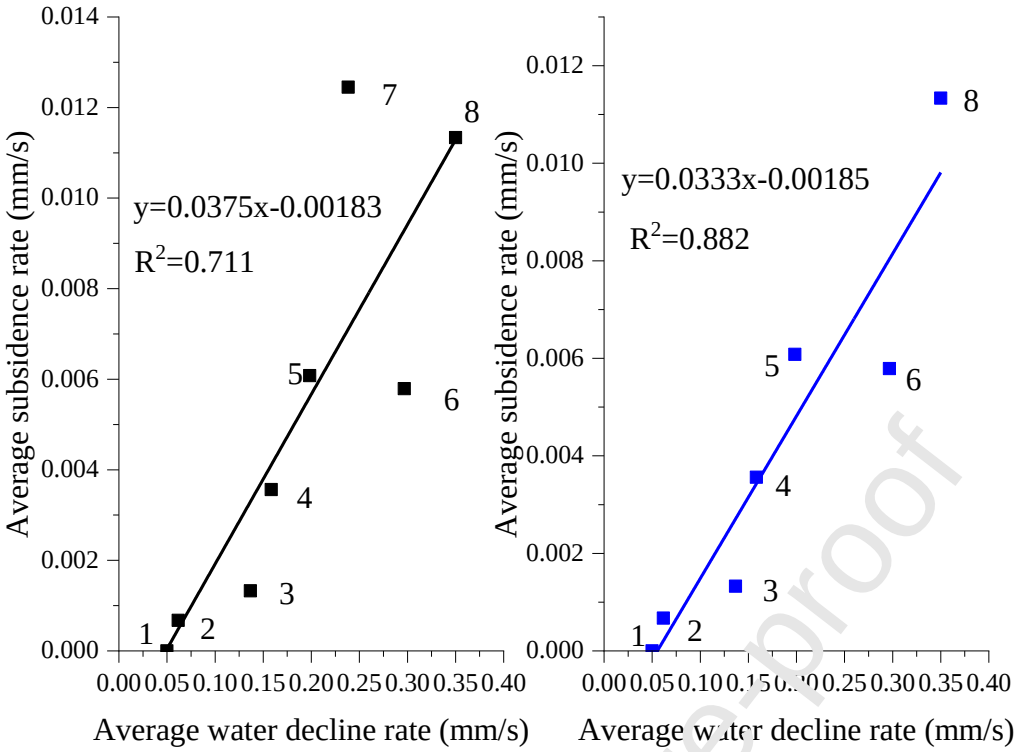

Figure 8. Plots showing the dependence between average water-level decline rate and average subsidence rate for the different tests. Values correspond to the whole test (stage 1 and 2) before the formation of a collapse. The plot on the right excludes test 7, characterised by an anomalous assymmetric subsidence in the initial part of the test (see profiles in Fig. 6).

5 Conclusions

The tests performed with a laboratory-scale physical model demonstrate that vacuum pressure induced by rapid water-table declines may trigger the development of sinkholes in a mantled karst setting comprising a cavernous bedrock overlain by a low-permeability cover. Real-time monitoring of the water level drawdown (magnitude, duration, rate), the negative air pressure in the bedrock cavity and the cover, and several features of the subsidence process (deformation style, size, magnitude, rate) revealed the following relationships between the vacuum pressure and the subsidence phenomenon:

- The critical stress threshold required for the initiation of subsidence in the cover may be exceeded by the combined effect of buoyancy loss and negative air pressure, in situations in which buoyancy loss alone would be insufficient to induce ground instability.
- Different subsidence styles may arise in the same cover depending on the patterns of the water-table decline (magnitude, duration, rate) and the associated vacuum pressures. In the tests performed in this work three main types of cover behavior were observed: sagging, sagging with fissuring and collapse, and sagging interrupted by early collapse. This variability can be attributed to some dependency between the water-table decline rates and the rheology of the cover, and to the critical effect of the development of fissures, which function as permeability features causing sharp changes in the negative air pressure values.
- There is a direct relationship between the water-level decline rates and the subsidence rate, especially when the sealing effect of the low-permeability cover is not disturbed by the development of throwgoing pathways for the air inflow (e.g., fissures).

The vacuum effect induced by water table drawdown most probably has a secondary local effect as a sinkhole trigger, compared to buoyancy loss. It requires the concurrence of low-permeability covers and rapid water level declines that may only occur close to pumping sites where cones of depressions reach the greatest depths. However, it may cause significant detrimental effects, especially at critical structures located in the vicinity of pumping sites. The results of these experiments provided the technical basis for proposing some possible alternatives for ameliorating its impact.

ACKNOWLEDGMENTS

This work was initiated with support from the National Natural Science Foundation of China NSFC Grant (No. 41502244) and was continued with support from the Fundamental Research Fund of SKLGP (No. SKLGP2018Z023). The work carried out by FG and JG has been supported by project CGL2017-85045-P funded Spanish Government.

Conflict of Interest: The authors declare that they have no conflicts of interest.

References

Abdulla, W.A., -Goodings, D. J. 1996. Modeling of sinkholes in weakly cemented sand. J. Geotech. Eng. 122(12), 998-1005.

Ali, H. Choi, J., 2020. Risk prediction of sinkhole occurrence for different subsurface soil profiles due to leakage from underground sewer and water pipelines. Sustainability. 12(1), 310.

Argentieri, A., Carluccio, R., Cecchini, F., Chiappini, M., Ciotoli, G., Ritis, R.D., Filippo, M.D., Nezza, M.D., Marchetti, M., Marchetti, S., Materni, V., Meloni, F., Nardi, A., Rotella, G., Sapia, V., Venuti, A., 2015. Early stage sinkhole formation in the Acque Albule basin of central Italy from geophysical and geochemical observations. Eng. Geol. 191, 36-47.

Augarde, C.E., Lyamin, A.V., -Sloan, S. W., 2003. Prediction of undrained sinkhole collapse. Journal of Geotechnical and Geoenvironmental Engineering. 129(3), 197-205.

Nam, B.H., , Shamet, R., -2020. A preliminary sinkhole raveling chart. Engineering Geology. 268, 105513.

Brinkmann, R., Parise, M., Dye, D., 2008. Sinkhole distribution in a rapidly developing urban environment: Hillsborough County, Tampa Bay area, Florida. Eng. Geol. 99 (3), 169-184.

Carbonel, D., Rodríguez, V., Gutiérrez, F., McCalpin, J.P., Linares, R., Roqué, C., Zarroca, M., Guerrero, J., Sasowsky, I., 2014. Evaluation of trenching, ground penetrating radar (GPR) and electrical resistivity tomography (ERT) for sinkhole characterization. Earth Surf Process Landf. 39, 214-227.

Chan, Y.C., 1994. Factors affecting sinkhole formation. Geotechnical Engineering Office, Civil Engineering Section. Hong Kong, GEO Report 28, pp. 46.

Chen, J., 1988. Karst Collapse in Cities and Mining Areas, China. Environmental Geology and Water Sciences. 12 (1), 29-35.

Chen, J., Xiang, S., 1991. Sinkhole collapse resulting from pumping of karst groundwater: a problem and its solution, in: Proceedings 4th International Conference on Land Subsidence, Houston, Publ IAHS Press, Wallingford, pp. 313-322.-

Craig, W.H., 1990. -Collapse of cohesive overburden following removal of support. Can. Geotech. J. 27(3), 355-364.

Doğan, U., Yılmaz, M., 2011. Natural and induced sinkholes of the Obruk Plateau and Karapınar-Hotamış Plain, Turkey. Journal of Asian Earth Sciences. 40(2), 496-508.

Chen, G., Chen, Y., Tan, H., 1993. A research in mechanism, prediction and remediation for karst collapse of ground soil. Proceedings Sixth International Congress IAEG Amsterdam, Vol. 3. Rotterdam, Balkema, pp. 1535-1542.

Gutiérrez, F., 2016. Sinkhole hazards. Oxford Research Encyclopedia of Natural Hazard Science. Oxford University Press, Oxford. pp 1-92

Gutiérrez, F., Benito Calvo, A., Carbonel, D., Desir, G., Sevil, J., Guerrero, J., Martínez-Fernández, A., Karamplaglidis, T., García-Arnay, Á., Fabregat, I., 2018. Review on sinkhole monitoring and performance assessment of the performance of remediation measures by high-precision leveling and terrestrial laser scanner in the salt karst of the Ebro Valley, Spain. Eng. Geol. 248, 283-308

Gutiérrez, F., Carbonel, D., Guerrero, J., McCalpin, J.P., Linares, R., Roqué, C., Zarroca, M., 2012. Late Holocene episodic displacement on fault scarps related to interstratal dissolution of evaporites (Teruel Neogene graben, NE Spain). Journal of Structural Geology. 34, 2-19.

Gutiérrez, F., Parise, M., Waele, J.D., Jourd, H., 2014. A review on natural and human-induced geohazards and impacts in karst. Earth-Science Reviews. 138, 61-88.

Jiang, F.W., Lei, M.T., Dai, J.L., Jia, L., Wu, Y.B., Luo, W.Q., 2015. Models of subsidence sinkhole in soils around reservoirs. Advanced Materials Research. 1065-1069, 575-579.

He, K., Wang, B., Zhou, D., 2004. Mechanism and mechanical model of karst collapse in an over-pumping area. Environmental Geology. 46(8), 1102-1107.

Khanlari, G.R., Heidari, M., Momeni, A.A., Ahmadi, M., Beydokhti, A.T., 2012. The effect of groundwater overexploitation on land subsidence and sinkhole occurrences, West of Iran. Quarterly Journal of Engineering Geology and Hydrogeology. 45, 447-456.

Lamoreaux, P.E., Newton, J.G., 1986. Catastrophic subsidence: an environmental hazard, Shelby county, Alabama. Environ. Geol. Water Sci. 8, 25-40.

Lei, M., Gao, Y., Jiang, X., 2015. Current Status and Strategic Planning of Sinkhole Collapses in China, in: Lollino, G., Manconi, A., Guzzetti, F., Culshaw, M., Bobrowsky, P., Luino, F. (Eds) Engineering Geology for Society and Territory. Springer, Cham, pp. 529-533. Lei, M., Jiang, X., Yu, L., 2002. New advances in karst collapse research in China. Environmental Geology. 42(5), 462-468.

Li, G., Zhou, W., 1999. Sinkholes in karst mining areas in China and some methods of prevention. Engineering Geology. 52, 45-50.

Linares, R., Roqué, C., Gutiérrez, F., Zarroca, M., Carbonel, D., Bach, Joan., Fabregat, I., 2016. The impact of droughts and climate change on sinkhole occurrence. A case study from the evaporite karst of the Fluvia Valley, NE Spain. Science of The Total Environment. 579, 345-358.Newton, J.G., 1984.

Sinkholes resulting from groundwater withdrawals in carbonate terrains, an overview. Rev. Eng. Geol., Geol. Soc. Am. 6, 195-202.

Parise, **M., 2019**. Sinkholes, in: White, W.B., Culver, D.C. Pipan, T. (Eds.), Encyclopedia of Caves. Academic Press, Amsterdam, Elsevier, 3rd edition, pp. 934-942.

Poppe, S., Holohan, E.P., Pauwels, E., Cnudde, V., -Kervyn, M., 2015. Sinkholes, pit craters, and small calderas: Analog models of depletion-induced collapse analyzed by computed X-ray microtomography. GSA Bulletin, 127(1-2), 281-296.

Romanov, D., Kaufmann, G., Al-Halbouni, D., 2020. Basic processes and factors determining the evolution of collapse sinkholes - A sensitivity study. Engineering Geology. 270, 105589.

Sevil, J., Gutiérrez, F., Zarroca, M., Desir, G., Carbonel, D., Guerrero, J., Linares, R., Roqué, C., Fabregat, I., 2017. Sinkhole investigation in an urban area by trenching in combination with GPR, ERT and high-precision leveling. Mantled evaporite karst of Zaragoza city, NE Spain. Eng. Geol. 231, 9-

Song, K., Cho, G.C., Chang, S.B., 2012. Identification, remediation, and analysis of karst sinkholes in the longest railroad tunnel in South Korea. Eng. Geol. 135-136, 92-105.

Taheri, K., Gutiérrez, F., Mohseni, H., Raeisi, E., Taheri, M., 2015. Sinkhole susceptibility mapping using the analytical hierarchy process (AHP) and magnitude–frequency relationships: A case study in Hamadan province, Iran. Geomorphology 234, 64-79.

Tharp, T.M., 1999. Mechanics of upward propagation of cover-collapse sinkholes. Engineering Geology, 52(1-2), 23-33.

Waltham, A.C., 1989. Ground subsidence. Chapman and Hall, New York.

Waltham, T., Bell, F., Culshaw, M., 2005. Sinkholes and Subsidence. Springer, Chichester.

Xu, W.G., Zhao, G.R., 1988. Mechanism and prevention of karst collapse near mine areas in China. Env. Geol. Water Sci. 12, 37-42.

Yang, M.Z., Drumm, E.C., 2002. Stability evaluation for the siting of municipal landfills in karst. Eng. Geol. 65 (2-3), 185-195.

Youssef, A.H., Al-Harbi, H.M., Gutiérrez, F., Zabramwi, Y.A., Bulkhi, A.B., Zahrani, S.A., Bahamil, A.M., Zahrani A.J., Otaibi Z.A., El-Haddad B.A., 2016. Natural and human-induced sinkhole hazards in Saudi Arabia: distribution, investigation, causes, and impacts. Hydrogeological Journal. 24, 625-644.

Youssef, A.M., Zabramwi, Y.A., Gutiérrez, F., Bahamil, A.M., Otaibi, Z.A., Zahrani, A.J., 2020. Geophysical investigation (ERT) of a sinkhole induced by uncontrolled groundwater withdrawl, Al Jouf Region, Saudi Arabia. Journal of Arid Environments, 177, 104132.

Zhou, W.F., 1997. The formation of sinkholes in karst mining areas in China and some methods of prevention. Environmental Geology. 31, 50-58.

Declaration of interests

☒ The authors declare that they have no known competing financial interests or personal relationships that could have appeared to influence the work reported in this paper.

☐The authors declare the following financial interests/personal relationships which may be considered as potential competing interests:

Authors of paper

ENGEO_2020_668, “The impact of groundwater drawdown and vacuum pressure on sinkhole development. Physical laboratory models”

declare that they have no competing interests

Xianxuan Xiao

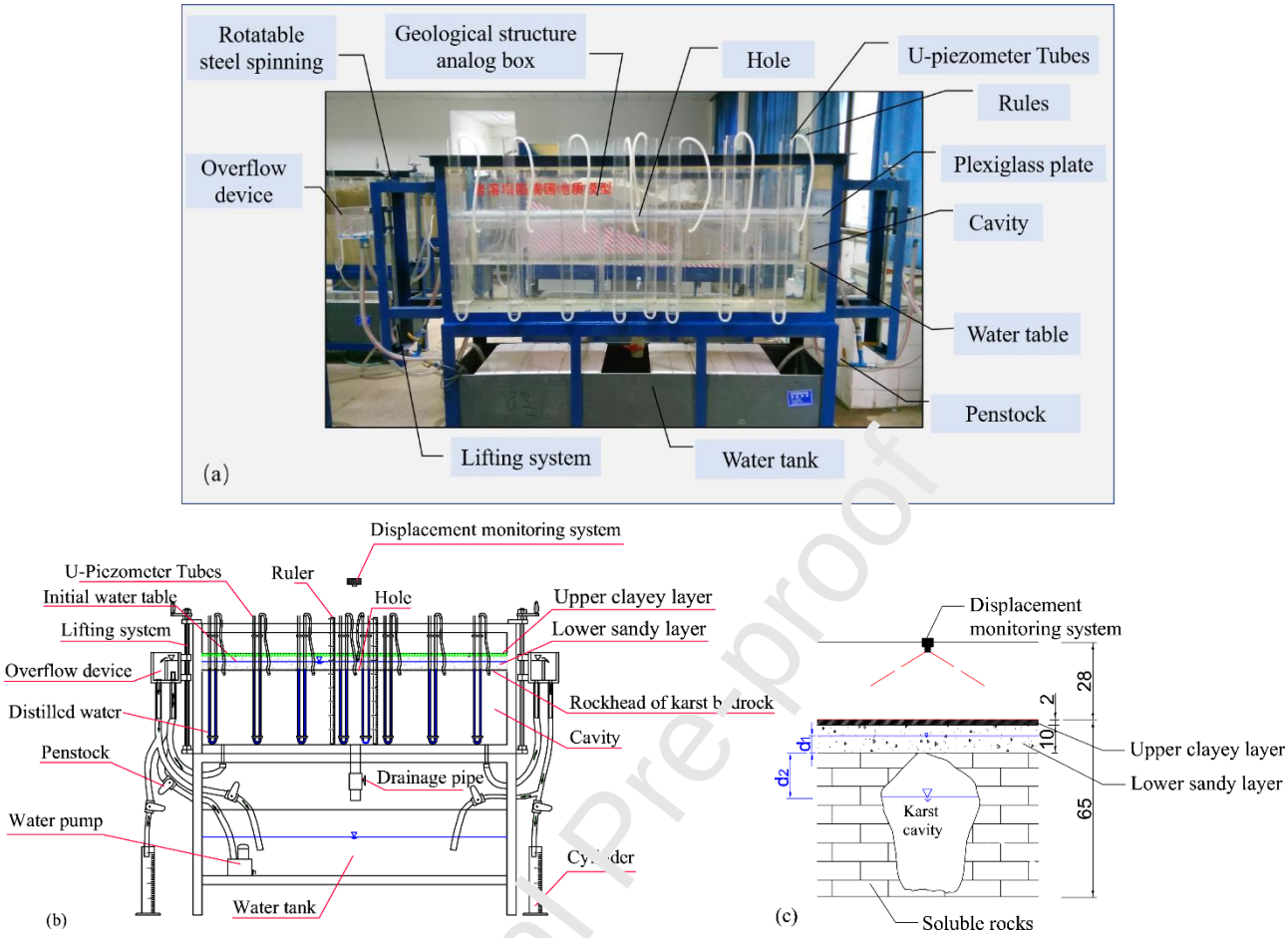

Figure 1. Illustrations of the experimental physical analog. (a) Photograph of the geological simulation box. (b) Sketch of the physical model showing the different components. (c) Idealized representation of the mantled karst setting simulated in the experiments, consisting of an unconsolidated cover with an upper low-permeability clayey seal and karst bedrock hosting a large cavity with an opening at the rockhead. See additional explanations in the text.

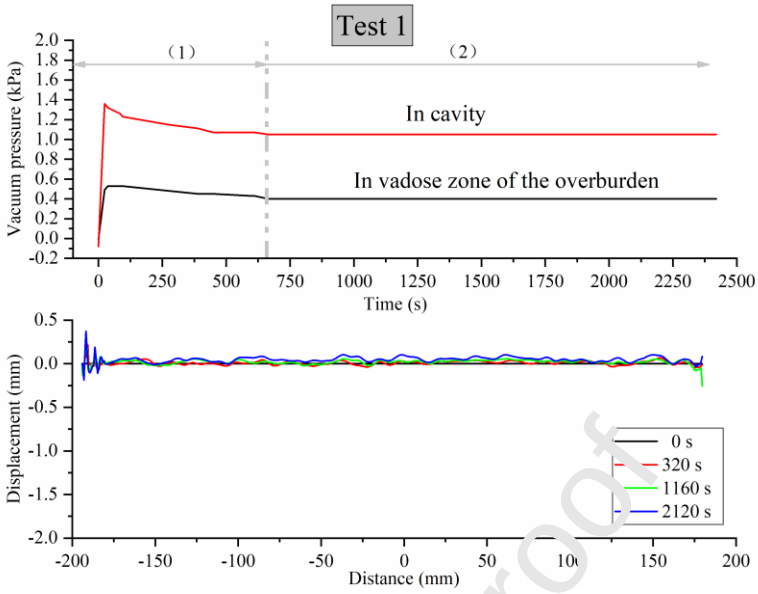

Figure 2. Data from test 1. The upper graph shows the negative air pressure recorded in the cavity and in the upper part of the sandy layer in the course of the water-level decline stages 1 and 2, labelled as (1) and (2). The lower graph shows the topographic profiles recorded at different times (two in stage 1 and two in stage 2), indicating no subsidence. The serrated pattern is related to the error margin of the measurements and the imperfect planar geometry of the ground surface.

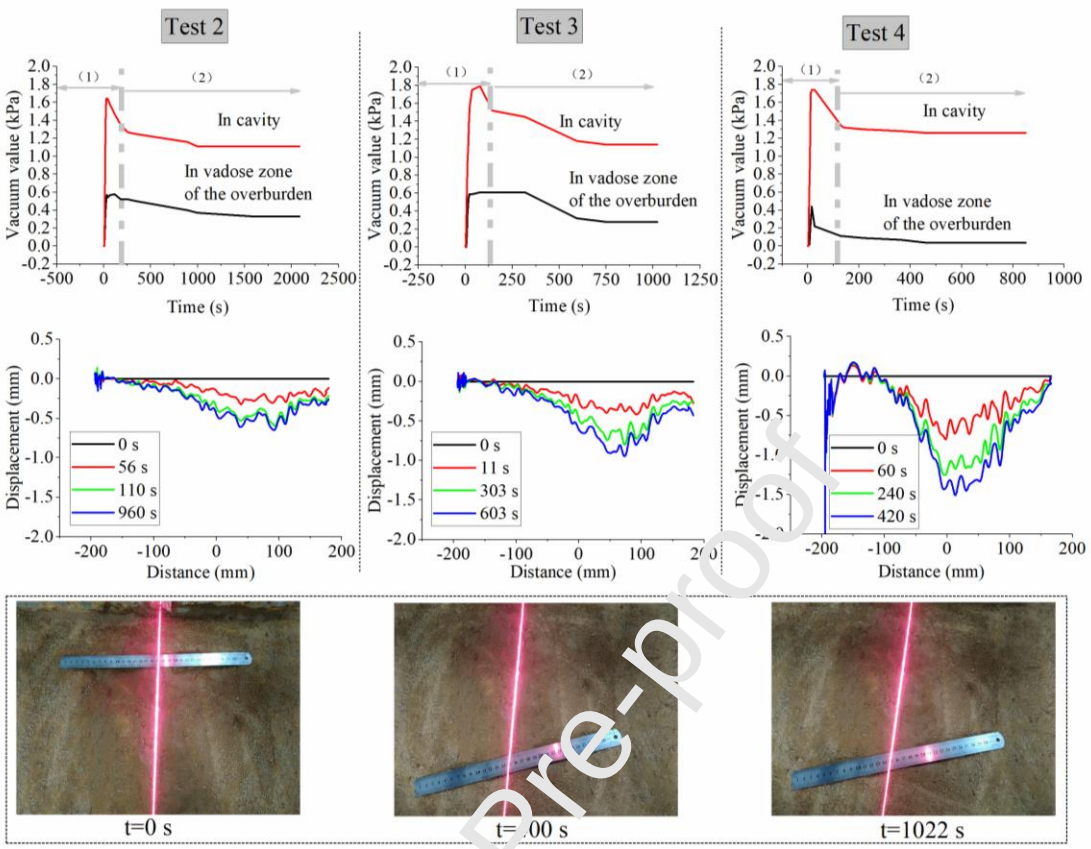

Figure 3. Data from tests 2, 3 and 4 characterized by sagging subsidence. The upper graphs show the negative air pressures recorded in the cavity and in the upper part of the sandy layer during the water-level decline stages 1 and 2. The lower graphs show the topographic profiles recorded at different times showing sagging subsidence and probably marginal bulging in test 4. The sequence of photographs corresponds to images taken at different times of test 3. They show the lack of fissure development during the experiment.

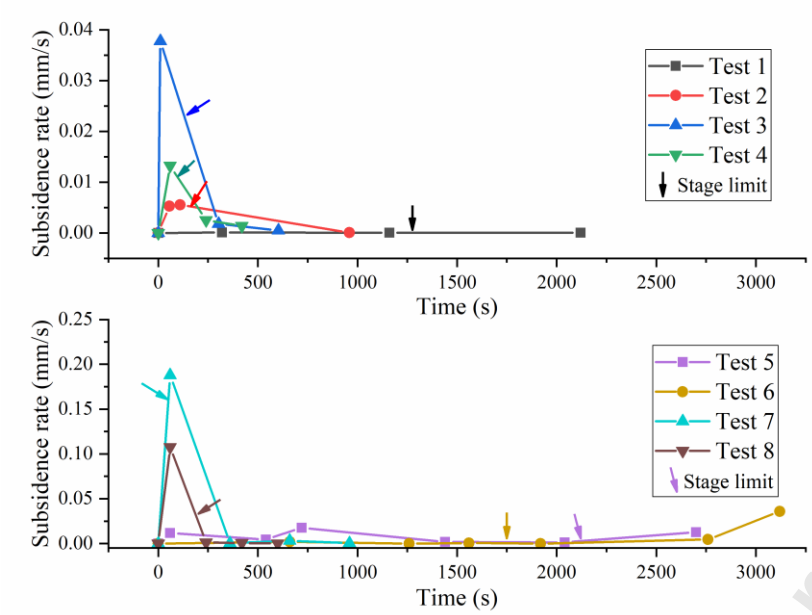

Figure 4. Subsidence rates computed for various time periods considering the vertical displacement at the point of maximum subsidence. Points are located at the end of each time lapse. Upper graphs show data from tests 1 to 4, and lower graph data from tests 5 to 8. Arrows point to boundary between stage 1 and 2.

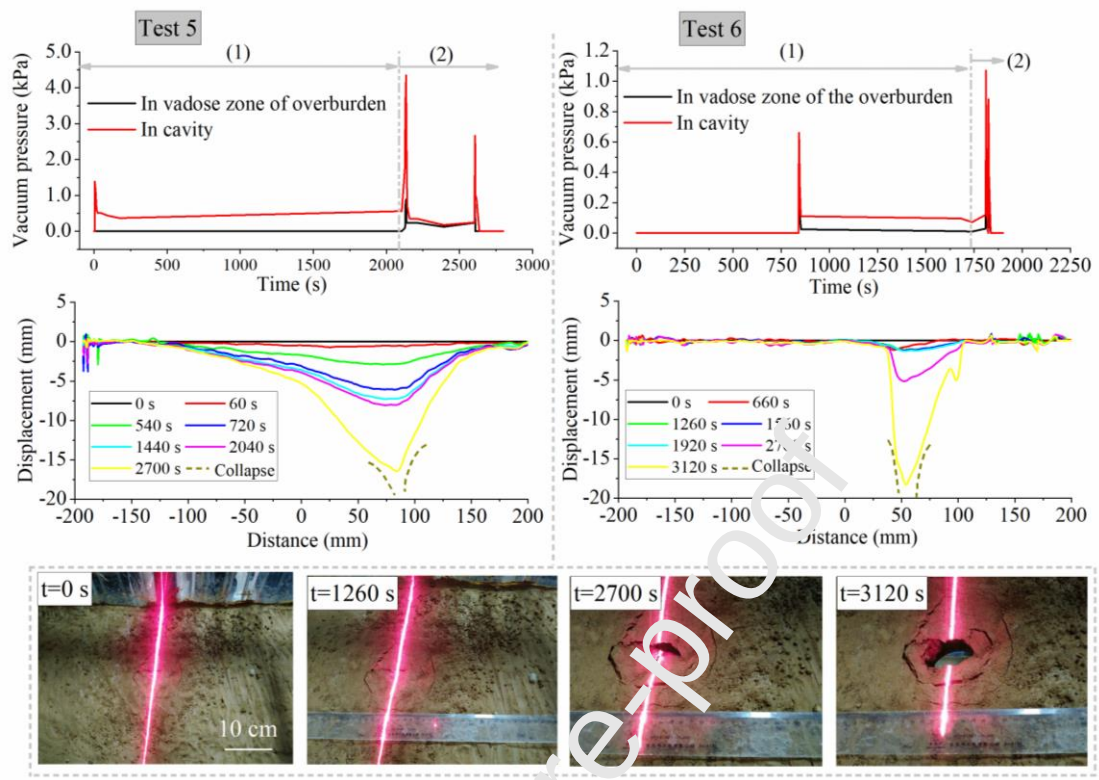

Figure 5. Data from Tests 5 and 6 characterized by prolonged sagging with cracking and collapse. The upper graphs show the negative air pressures recorded in the cavity and in the upper part of the sandy layer during the water-level decline stages 1 and 2. The lower graphs show the topographic profiles recorded at different times before the development of the final collapse. The sequence of photographs corresponds to images taken at different times of Test 6.

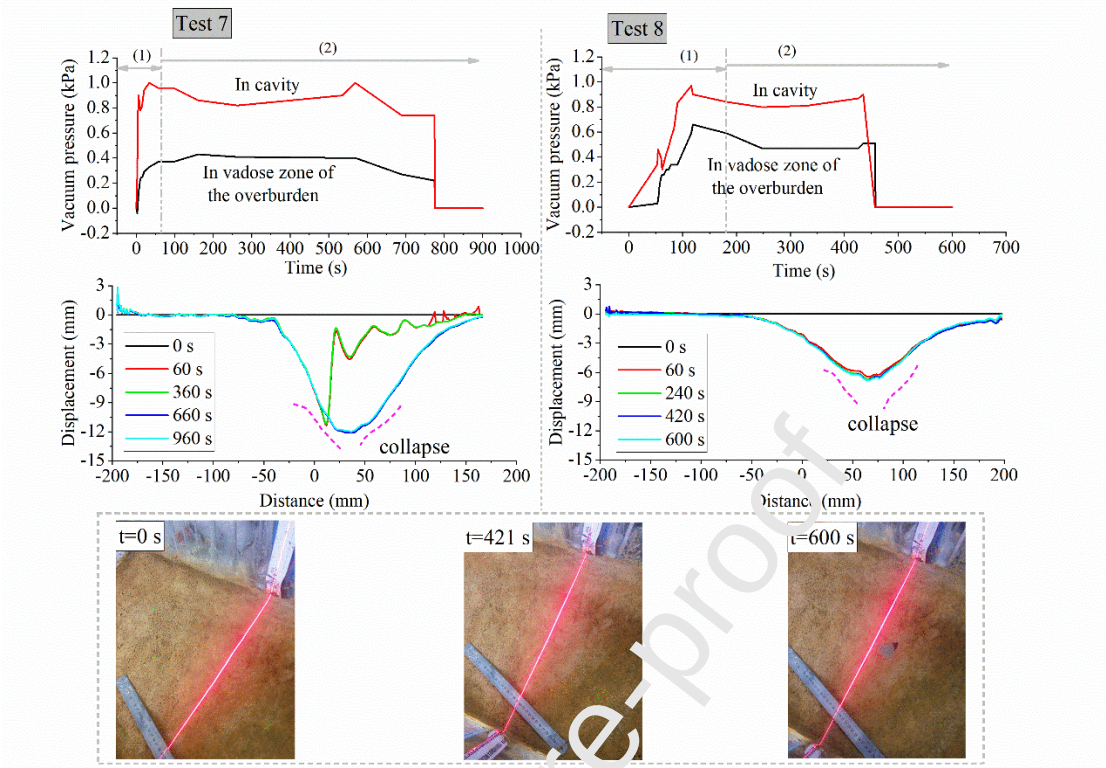

Figure. 6 Data from tests 5 and 6 characterized by prolonged sagging with cracking and collapse. The upper graphs show the negative air pressures recorded in the cavity and in the upper part of the sandy layer during the water-level decline stages 1 and 2. The lower graphs show the topographic profiles recorded at different times before the development of the final collapse. The sequence of photographs corresponds to images taken at different times of test 8.

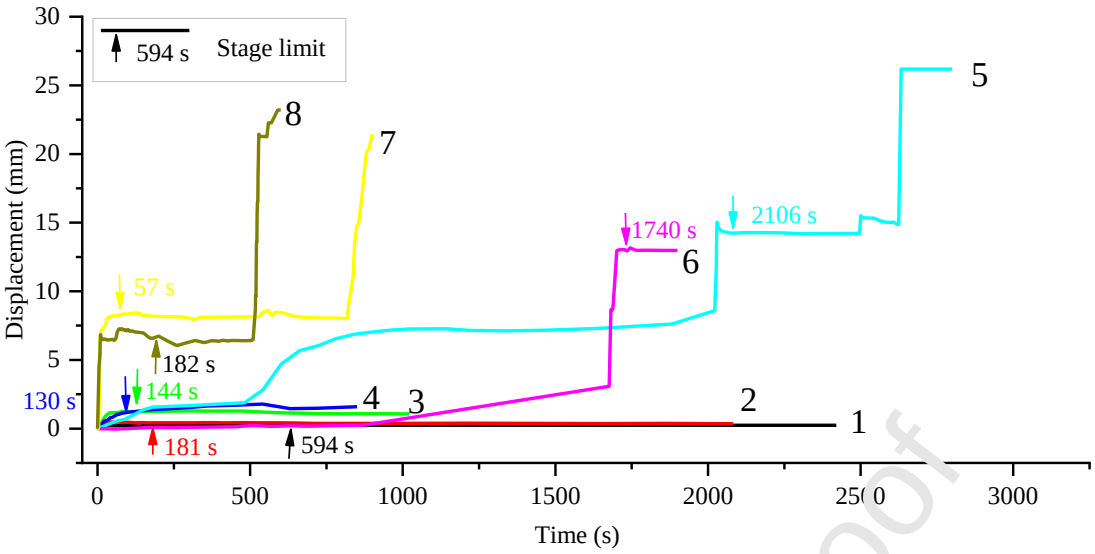

Figure 7. Plot showing cumulative displacement versus time for the different tests.

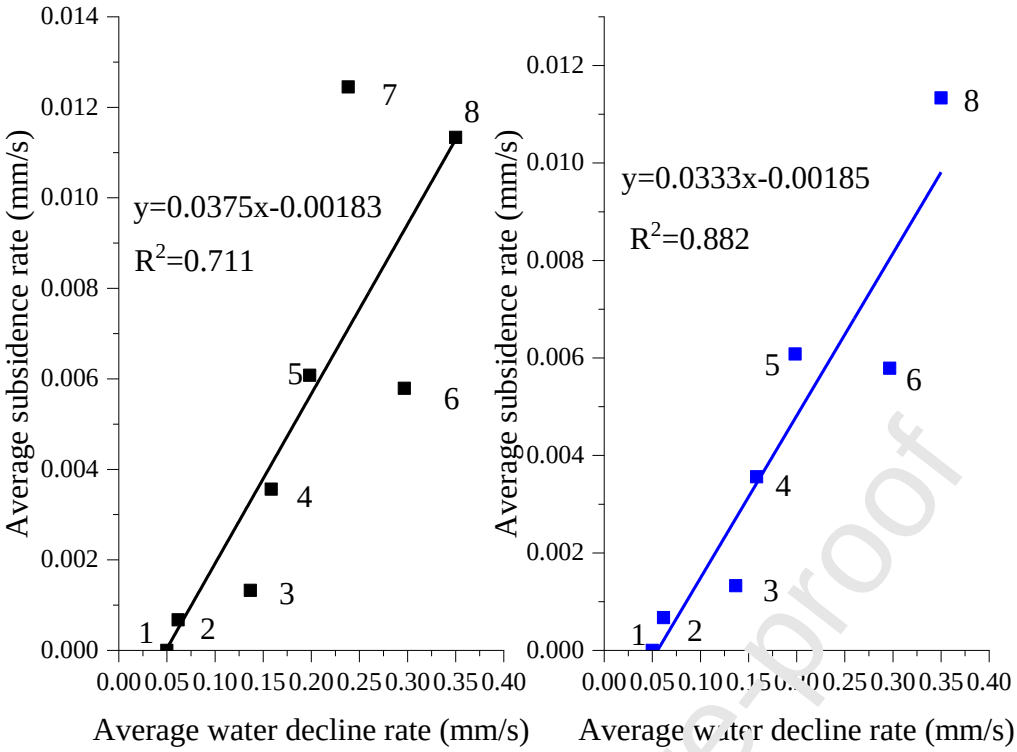

Figure 8. Plots showing the dependence between average water-level decline rate and average subsidence rate for the different tests. Values correspond to the whole test (stage 1 and 2) before the formation of a collapse. The plot on the right excludes test 7, characterised by an anomalous assymmetric subsidence in the initial part of the test (see profiles in Fig. 6).

Highlights

- Vacuum pressure triggers collapse sinkholes in karstic areas with low-permeability covers.
- Different water-table decline patterns result in different cover subsidence styles.
- Ground fissuring may diminish the vacuum effect.
- Vacuum suction and subsidence show a positive correlation with rapid water level drawdowns and low-permeability covers.